IEEE Journal of Microwaves

Received 13 October 2022; revised 24 November 2022 and 16 January 2023; accepted 21 February 2023. Date of publication 15 March 2023; date of current version 7 April 2023.

Digital Object Identifier 10.1109/JMW.2023.3250340

Compact and Digitally Controlled D-Band Vector Modulator for Next-Gen Radar Applications in 130 nm SiGe BiCMOS

JONATHAN WITTEMEIER [1] (Graduate Student Member, IEEE), MUHAMMED ALI YILDIRIM [1] (Graduate Student Member, IEEE), AND NILS POHL [1,2] (Senior Member, IEEE)

(Invited Paper)

[1]Institute of Integrated Systems, Ruhr University, 44801 Bochum, Germany
[2]Fraunhofer Institute for High Frequency Physics and Radar Techniques, 53343 Wachtberg, Germany

CORRESPONDING AUTHOR: Jonathan Wittemeier (e-mail: jonathan.wittemeier@rub.de).

This work was supported by the German Research Foundation [Deutsche Forschungsgemeinschaft (DFG)] under Project-ID 287022738 TRR 196 for Project C03.

ABSTRACT Radar systems got very popular in sensing applications in the last two decades besides the traditional military sector. Nowadays, many applications favor multiple-input multiple-output (MIMO) radar over phased-array radar. Here, time-division multiplexing (TDM) and code-division multiplexing (CDM), like a phase-modulated continuous wave (PMCW), are well-known techniques. However, every method needs special components on the MMIC. In this article, a 125 GHz vector modulator (VM) circuit is presented, which can operate as a switchable amplifier in TDM systems, as a binary-phase modulator in CDM systems, and as a phase-shifter in phased-array systems. Based on simulations and S-parameter measurements, the VM itself and the three different operating modes are analyzed. We also present a technique to separate coupler imperfections from the S-parameter measurements to analyze the VM separately. We designed the VM with the B11HFC silicon-germanium technology ($f_t/f_{max} = 250/370$ GHz), using both HBTs (heterojunction bipolar transistors) and CMOS transistors. Inside the VM, two cross-connected power amplifiers (PAs) are fed by an in-phase (I), and two cross-connected PAs are fed by a quadrature-phase (Q) signal. The four PAs are controlled by a 4-bit interface to switch them on or off, thus generating output signals in the range of 0° to 360°.

INDEX TERMS MTT 70th Anniversary Special Issue, BiCMOS, BPSK, CDM, code-division, D-band, DDMA, doppler-division, MIMO, multiple-input multiple-output, phase-coded, phase-shifter, phased-array, PMCW, radar, SiGe, silicon-germanium, TDM, time-division, vector modulator, VM.

I. INTRODUCTION

A key driver in research on radar systems is the automotive industry. More than two decades ago, 24 GHz was the starting point, but nowadays, 77 GHz is widely used [1]. Future radar systems are targeting several goals. Besides more available bandwidth, a smaller MMIC size is desired. To fulfill this requirement, future radar sensors will target the D-band [1], [2], [3], [4], [5]. Hereby, the MMIC size, antenna size, and antenna spacing d, and, therefore, the overall sensor size shrink due to the smaller wavelength λ. To compensate for the smaller antenna aperture and the increased free-space loss at high frequencies, a higher antenna count N is targeted. In summary, if the array size $(N \cdot d)$ stays the same, according to the Rayleigh criterion, the angular resolution increases [6, p. 45], and the robustness against noise is enhanced [7]. Also, with a higher center frequency (e.g., using frequency multiplication) the absolute bandwidth will increase when the same relative oscillator's tuning range is used. Therefore, the range resolution will increase. Besides this, the THz frequency range beyond 300 GHz is a long-term goal in

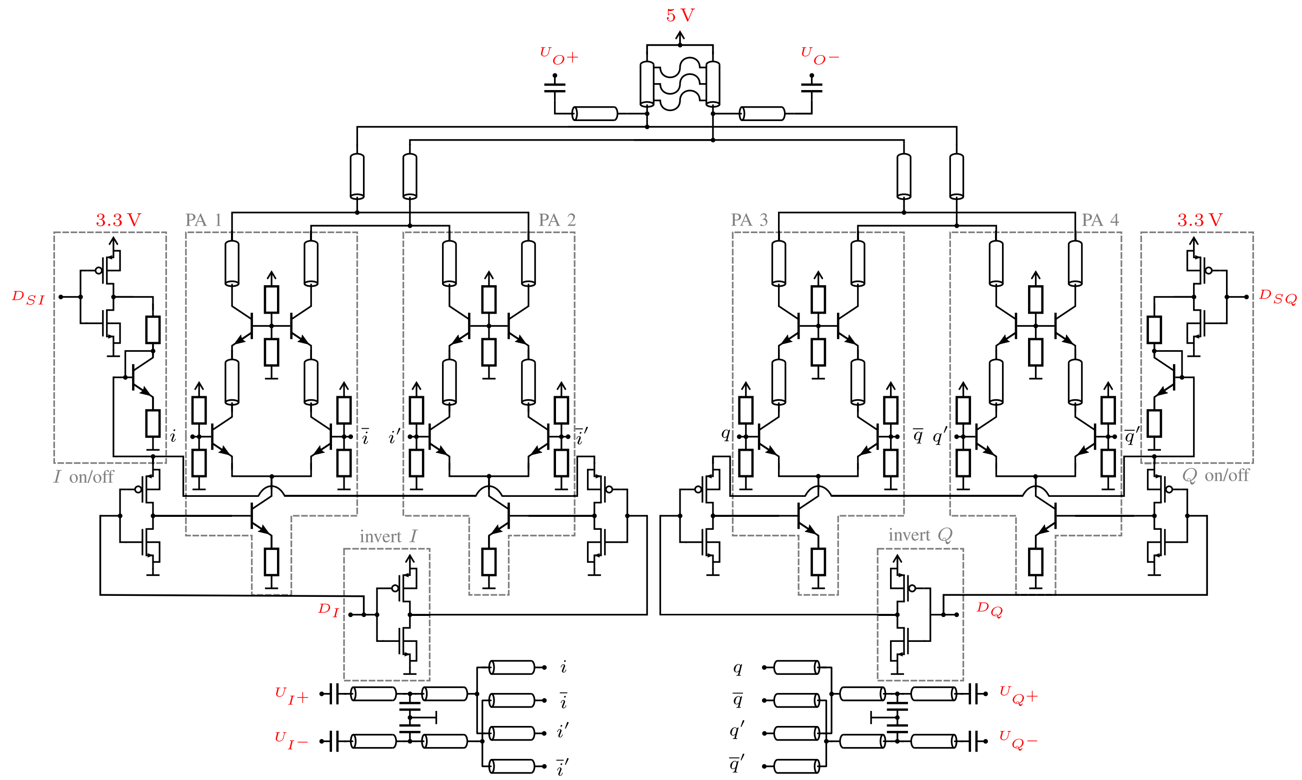

FIGURE 1. 125 GHz vector modulator circuit diagram, which is based on two pairs of cross-connected PAs and on a CMOS-based control circuit. Each pair uses the same input signal (I or Q), and all use the same inductive load.

applications where large bandwidth is required [8], [9], [10], [11].

Modern radar systems also evolve in terms of flexibility. Concepts with integrated communication [12], [13], [14], switchable operation mode [15], and DDS-based complex modulations schemes [16], [17] have been presented. Especially PMCW and DDMA radar get more attention over time, because of the robustness against interference between multiple radars [18], [19], [20] and better velocity estimation [21], respectively.

A key component in multi-channel radar systems is the vector modulator (VM). Based on system requirements, an on-off switch inside the last stage of a TDM system [22], [23], [24], [25], binary phase-shifter for phase-coded systems [1], [18], [26], [27], [28] or a phase-shifter for phased-array systems [29], [30], [31] is needed. The most common approaches using SiGe for designing a VM are variable gain amplifiers (VGAs) in combination with multiple coupler paths or switching elements [32], [33], [34], [35], [36], [37], Gilbert Cells (GCs) with analog tuning voltages [38], [39], [40], [41], [42], [43], [44], [45], [46], [47], [48], [49], [50], and reflection type phase-shifters [51], [52], [53], [54]. Besides that, GCs with on-chip digital-analog converters (DACs) [55], [56], switchable delay lines [57], modified Doherty amplifier [58], modified GCs [59], and tunable attenuators [60] have been presented. Moreover, there are many published BPSK modulator circuits [61], [62], [63], [64].

The presented vector modulator circuit targets future D-band FMCW radar systems to enable more flexibility. It provides a fully digital interface similar to [65], [66]. Hereby, fast phase state changes are possible to enable PMCW radar operation to enhance interference mitigation properties. TDM MIMO radar operation is enabled by switching the VM on/off such that only one radar transmitter is enabled at a given time, and phased-array operation is enabled by controlling the VM's output phase. For all three operation types, the same 4-bit interface is used. Therefore, no DAC is needed to produce these different modulation schemes.

The article is divided into several sections. First, Section II presents the circuit design of the VM and the architecture of the breakout MMIC. In Section III, the simulation results are shown. Afterward, the measurement results and a technique to isolate the coupler's imperfections are presented in Section IV. To show the vector modulator's capabilities, phased-array, and PMCW properties are examined in Sections V and VI, respectively. The article is concluded in Section VII.

II. 125 GHZ VECTOR MODULATOR DESIGN

The complete circuit diagram of the 125 GHz VM is shown in Fig. 1. All external signals are shown in red and relevant internal signals in black. The vector modulator is based on four parallel PAs, where every PA is working on a common load. Two PAs share the in-phase (I) input signal U_I and two PAs share the quadrature-phase (Q) input signal U_Q (cf. Fig. 2). The HBT's base signals i, $\bar{i}$, i', and $\bar{i}'$ and the circuitry of the collectors of the common-base stage are arranged in such a way that a 180° inversion of the I signal can take place.

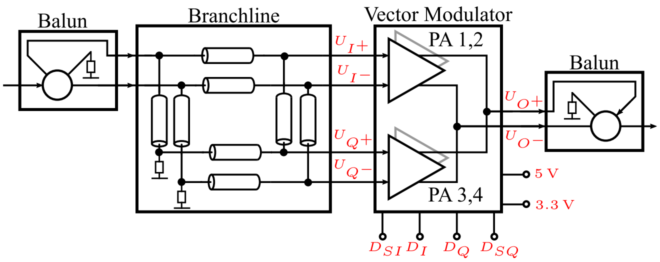

FIGURE 2. Block diagram of the breakout MMIC.

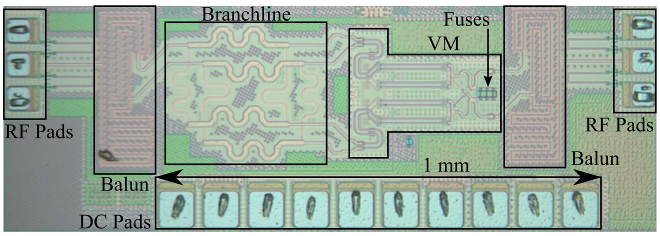

FIGURE 3. Micro-photograph of the breakout MMIC.

The same applies to the transistors in the Q path. By using the common output (U_O), it is possible to achieve eight phase states in the range of 0° to 360°. For this, the control signals D_{SI}, D_I, D_Q, and D_{SQ} are used. In summary, eight different phase states can be generated, and a ninth state is possible, where the VM is turned off.

Inside the VM, HBTs with an emitter length of 4 μm are used for RF amplification and 3.3 V compatible CMOS transistors for controlling the phase states. The input matching network consists of a series capacitance, a parallel capacitor connected to signal ground, and a splitting structure. The split I and Q signals are fed to the four differential amplifiers. Each differential amplifier has its own current mirror that can be switched off, a common-emitter stage, and a common-base stage. Between the two stages, transmission lines (TRL) are used for interstage matching to enhance RF performance [67].

The differential inductive load consists of two short ($< \lambda/4$) TRLs connected to the 5 V node, which are utilized as inductors. The inductive load can be trimmed with a laser by cutting laserfuses in the top metal layer. Up to three fuses can be removed, which leads to four different inductive loads (cf. Fig. 3). The output TRL and capacitance, connected to U_O, are designed to provide a good matching to $Z_{\text{diff}} = 100\,\Omega$.

While the RF HBTs are supplied with 5 V, the CMOS part is supplied with 3.3 V. Here, the signals D_{SI} and D_{SQ} are used to turn on or off the I and Q path inside the VM, respectively. The D_I and D_Q signals are used to invert the I and Q signals, respectively. In this case, one amplifier inside the I or Q path is switched off completely, and the cross-connected one is turned on. A corresponding CMOS inverter circuit ensures that only one amplifier is active within the I or Q path of the VM. In summary, only a maximum of two of the four amplifiers are active at the same time.

The rectangular size of the VM is 260 μm by 330 μm (0.085 mm^2). After the input stage, the width shrinks from 260 μm to 160 μm. Therefore, the non-rectangular size is $160\,\mu\text{m} \cdot 330\,\mu\text{m} + 2 \cdot 50\,\mu\text{m} \cdot 80\,\mu\text{m} = 0.0608\,\text{mm}^2$. For a compact design, differential TRLs for the input matching are designed in a meander structure. The interstage matching between the common-emitter and the common-base stage also uses differential TRLs. The signal combination, the inductive load, and the output matching are designed with single-ended TRLs.

A. ARCHITECTURE OF THE BREAKOUT MMIC

The block diagram of the MMIC and the breakout chip are shown in Figs. 2 and 3, respectively. Here, the single-ended pads, two baluns implemented as compact rat-race couplers, a TRL-based branchline coupler, and the vector modulator circuit are shown. The MMIC's size is $1450\,\mu\text{m} \cdot 500\,\mu\text{m} = 0.725\,\text{mm}^2$.

Single-ended probing pads are used, which are tuned to 125 GHz by using a resonant TRL against ground. This transforms the lowpass behavior of the pads into bandpass behavior. The couplers have meander designs to achieve compact dimensions. The breakout chip has ten dc pads to supply and control the modulator. These include three ground pads, one 3.3 V pad, one 5 V pad, four digital control pads, and one pad to tune the HBT's current density by changing the 3.3 V supply voltage in the I/Q on/off path. Between the components on the breakout chip, bypass capacitors are placed to ensure a stable supply voltage.

III. SIMULATION RESULTS

The targeted center frequency of the vector modulator is 125 GHz. Therefore, all subsequent plots are aligned to this and show a bandwidth of 30 GHz. It is particularly important that the coupler's amplitude and phase errors are minimal. Phase errors, e.g. non-ideal 90° phase difference between I and Q, have a direct effect on the performance of the VM, since a vector superposition is performed at the PA outputs. Therefore, all other constellation points will have non 45° phase difference. Also, a difference in amplitude between the I and Q signal will tilt four out of eight constellation points (±I ± Q) towards the stronger signal.

A. COUPLER SIMULATION

For a detailed investigation of the couplers, Sonnet version 18.52 together with a 2-layer thick metal sheet model was used [68]. The simulation results of the branchline coupler and the balun are shown in Figs. 4 and 5, respectively. The branchline's best input matching is achieved at ≈ 134 GHz. The ideal phase difference of 90° is at ≈ 139 GHz. An amplitude difference of ≈ 5 dB is achieved in the shown frequency range. Typically, IQ amplitude differences are below 2 dB in this frequency range [32], [36], [44]. Here, the slightly higher amplitude difference and center frequency are caused by the TRL width and length choice, respectively. The suboptimal

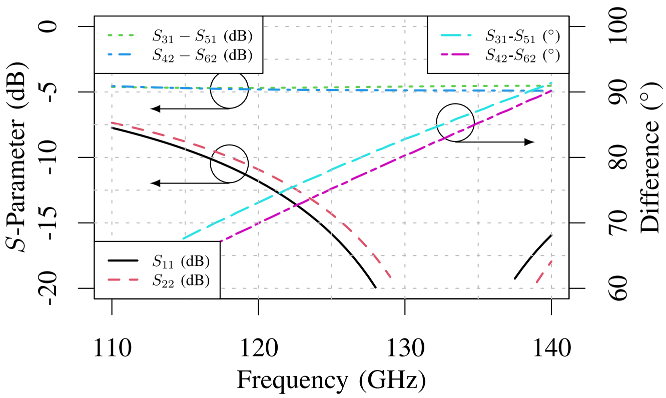

FIGURE 4. Sonnet simulation results of the TRL based branchline coupler. Despite the higher center frequency and amplitude imbalance, the branchline coupler can be used.

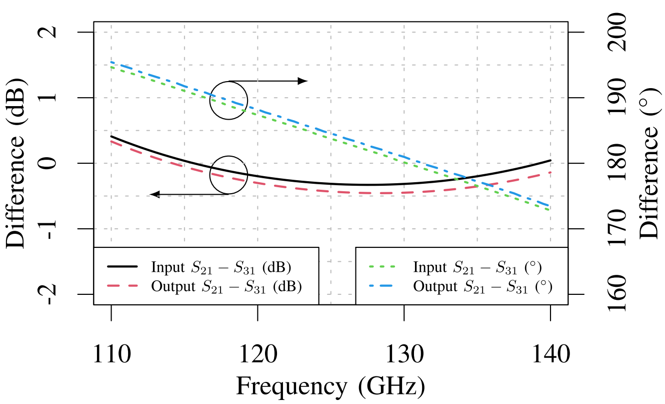

FIGURE 5. Sonnet simulation results of the differential ports of the TRL based input and output balun.

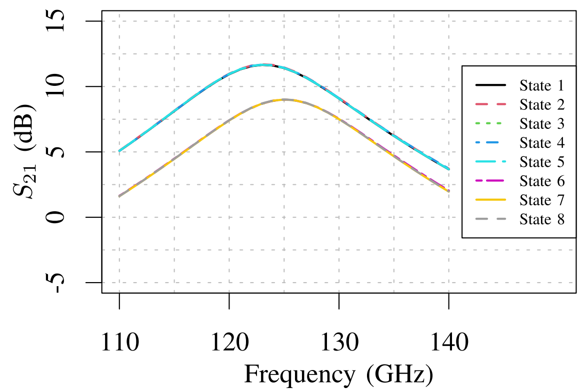

FIGURE 6. S_{21} (dB) simulation results of the VM using an ideal differential branchline coupler, RC parasitics, and differential ports.

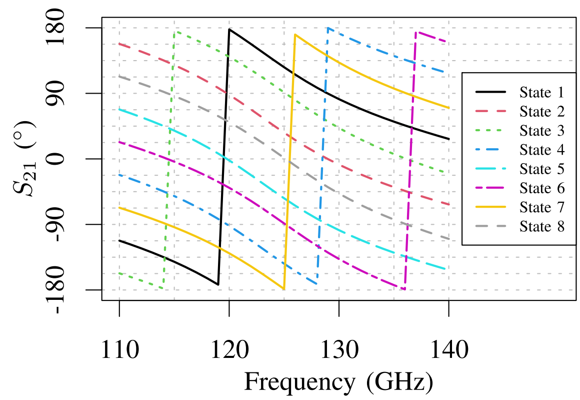

FIGURE 7. S_{21} (°) simulation results of the VM using an ideal differential branchline coupler, RC parasitics, and differential ports.

choices were detected after MMIC production, and the effects will be examined in more detail in the next Sections.

In contrast to the branchline coupler, the rat-race baluns operate closer to the targeted center frequency. The two most important characteristic values of a balun, the phase and amplitude imbalance at the balanced outputs, are shown in Fig. 5. The balun at the input of the breakout chip is analyzed as well as the balun at the output of the breakout chip. While both baluns are identical, they differ in TRL length at the balanced ports, which are also simulated (cf. Fig. 3). Both baluns have an amplitude imbalance of less than 0.5 dB in the shown frequency range. An amplitude difference of 0 dB is achieved at ≈ 115 GHz and ≈ 140 GHz. As with the branchline coupler, the ideal phase difference is achieved at a slightly higher frequency, namely ≈ 131 GHz. For both baluns, S_{11} is below 20 dB, and the insertion loss is less than 1.65 dB in the range from 110 GHz to 140 GHz, respectively.

B. VECTOR MODULATOR SIMULATION

After the couplers have been described, the VM including the couplers are examined. Here, the VM's schematic (cf. Fig. 1) and extracted RC parasitics using Mentor Calibre are used. The simulations consider a device temperature of 80 °C. Two types of simulations are performed. First, an ideal branchline coupler and differential ports are used. The ideal branchline coupler splits the input signal without additional losses, has perfect port matching, and constant 90° IQ outputs. Second, the S-parameter data for all three couplers from the Sonnet simulations are used together with single-ended ports. Then the results of both analyses are compared in a constellation diagram (Section III-C).

Fig. 6 shows the results of the harmonic balance based S-parameter simulation (−15 dBm input power), which considers non-linearity (e.g. compression effects). It can be seen that two different gain curves are obtained. The maxima are in the range of 125 GHz. The length of the TRL based inductive load was chosen as if one fuse had been removed (cf. Fig. 3). A maximum gain of 11.70 dB and a minimum gain of 8.99 dB is achieved, respectively.

The simulated phase curves are shown in Fig. 7. Here, it can be seen that the 45° phase difference could be achieved very well. A more detailed representation can be seen later in Fig. 10.

Fig. 8 shows the simulation results when Sonnet's results are used. Due to the IQ imbalance of the branchline coupler, four different gain curves are visible. In addition, the gain is reduced since the couplers have losses which Sonnet

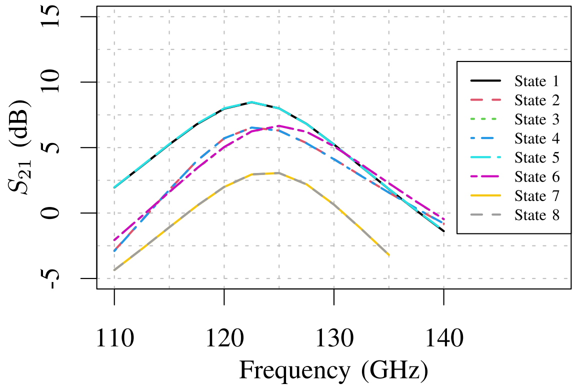

FIGURE 8. S_{21} (dB) simulation results of the VM using simulated couplers, RC parasitics, and single-ended ports.

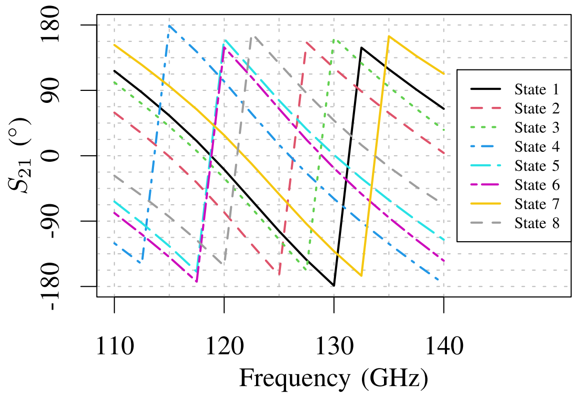

FIGURE 9. S_{21} (°) simulation results of the VM using simulated couplers, RC parasitics, and single-ended ports.

also considers. Also, non-ideal differential signals lead to a reduced gain because of the common-mode rejection of the differential amplifiers. Therefore, a maximum gain of 8.48 dB and a minimum gain of 3.05 dB is achieved, respectively. A suppression of the input signal of ≈ 80 dB is achieved when the VM is switched off completely.

When looking at the phase in Fig. 9, it is noticeable that the spacing between the individual VM states has become irregular because the simulated branchline coupler does not generate ideal IQ signals.

C. CONSTELLATION DIAGRAM AT 125 GHZ

In the constellation diagram in Fig. 10, the differences of both simulations at 125 GHz can be compared. The coupler's losses, the IQ imbalance, and the amplitude imbalance can be determined directly. The radial axis shows the gain, and the circular axis the phase. Here, the ticks of the radial axis are shown as concentric circles starting at 0 dB and increasing in 5 dB steps.

First, it is noticeable that with the ideal couplers, a higher gain is achieved. Second, the four phase states where both I and Q are active are tilted $\approx 10°$ clockwise to the states where only I or Q are active. This effect is nearly invisible when RC parasitics are ignored (not shown in Fig. 10). Also, without

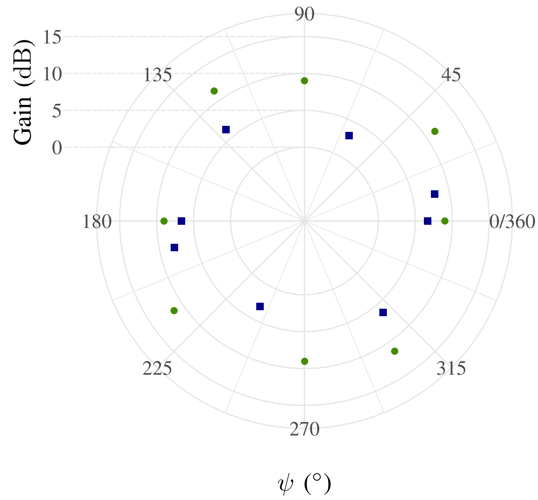

FIGURE 10. Constellation diagram at 125 GHz of the vector modulator using an ideal differential branchline coupler and the Sonnet simulation results, respectively.

RC parasitics, the difference between one and two active PAs is almost 3 dB. With RC parasitics, the difference is lowered to ≈ 2 dB. Thus, RC parasitics affect the linearity of the VM negatively.

When using Sonnet's S-parameter data, the non 90° phase difference between I and Q as well as the amplitude imbalance is visible. Because of the superposition of I and Q, constellation points with two active PAs are tilted even more. Two different metrics are important when looking at a constellation diagram: The root-mean-square (RMS) phase error (1) and the RMS amplitude error (2).

$$\Delta\varphi = \sqrt{\frac{1}{N} \cdot \sum_{n=1}^{N=8} (\varphi(n) - \varphi_{ideal}(n))^2} \tag{1}$$

$$\Delta A = \sqrt{\frac{1}{N} \cdot \sum_{n=1}^{N=8} (A(n) - A_{ideal}(n))^2} \tag{2}$$

Here, N is the number of states, $A(n)$ and $\varphi(n)$ are the achieved amplitude and phase values, and $A(n)_{ideal}$ and $\varphi_{ideal}(n)$ are ideal amplitude and phase values for a specific state. The presented VM circuit where I and Q are superimposed should achieve an RMS amplitude error of 1.5 dB because four of the eight states have 3 dB more gain. When using the ideal couplers, an RMS phase error of 5.2° and an RMS amplitude error of 1.21 dB is achieved, which is below the above-mentioned 1.5 dB. The reason for this is the non-ideal vector superposition at the output of the VM. When using the S-parameter files from Sonnet, an RMS phase error of 14.35° and an RMS amplitude error of 1.81 dB is achieved. Based on the findings in Sections V and VI, these values are satisfactory for beam-steering and PMCW radar.

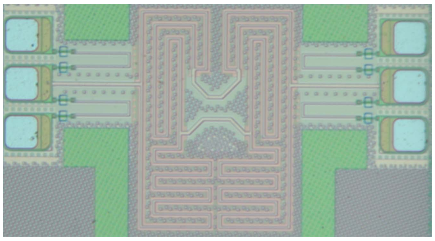

FIGURE 11. Micro-photograph of the back-to-back structure.

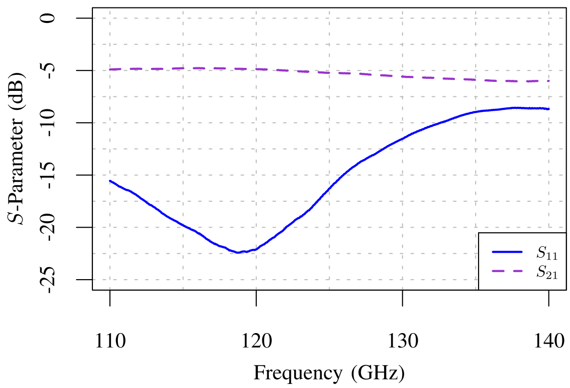

FIGURE 12. *S*-parameter measurement results of the balun back-to-back structure.

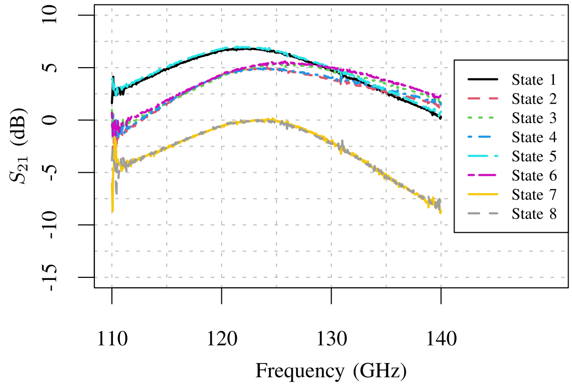

FIGURE 13. S_{21} **(dB) measurement results of the VM when no fuses are cut (compensated pad and balun losses).**

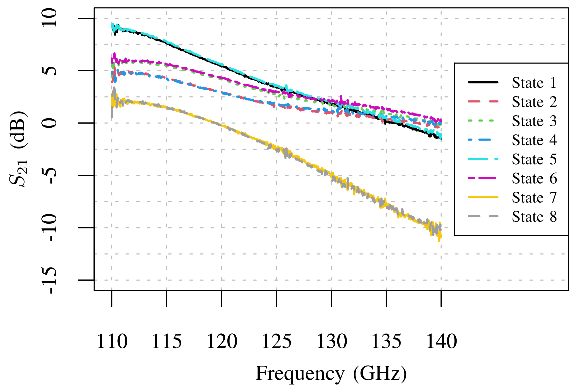

FIGURE 14. S_{21} **(dB) measurement results of the VM when one fuse is cut (compensated pad and balun losses).**

IV. MEASUREMENT RESULTS

S-parameter measurements of the above-mentioned circuits were performed with a Keysight PNA-X N5247B vector network analyzer (VNA) and VDI D-band extenders. An extender with an integrated attenuator was used on the input side so that the VM and its gain are not distorted by compression effects. Also, an analysis of the compression behavior is performed in Section IV-C.

A. S-PARAMETER MEASUREMENT RESULTS

To examine the gain of the VM in more detail, the losses of the pads and baluns are subtracted. For this purpose, a back-to-back structure was created (Fig. 11) to measure the insertion loss of the baluns and pads [69].

Fig. 12 shows the measurement results of the back-to-back structure. After calibrating the VNA, including extenders and probes, with an off-chip SOLT calibration substrate, it can be seen that the baluns and pads cause ≈ 5 dB losses at the center frequency. The best matching of the baluns and pads is just below 120 GHz and below 20 dB.

The *S*-parameter measurements of the VM are performed for different fuse configurations. Up to three fuses can be removed. Therefore, four different measurement scenarios can be examined. However, since the center frequency is already below 110 GHz after removing two fuses, only three fuse configurations are discussed below. The branchline coupler's insertion loss cannot be subtracted from the *S*-parameter measurements since there is no back-to-back structure. Therefore, the subsequent plots focus on the S_{21}-parameter because the S_{11}-parameter is mainly determined by the branchline coupler, and the minimum of S_{22} is strongly correlated with the maximum of S_{21}.

Figs. 13 to 15 show the gain curves of the VM. When no fuse is removed, the center frequency is at ≈ 121 GHz. A maximum gain of 7.01 dB and a minimum gain of 0.03 dB is achieved at this frequency. When one laserfuse is removed from the inductive load, the center frequency drops, and is about ≈ 110 GHz. As already shown in Section III-B, four different gain curves are measured due to the IQ imbalance of the couplers.

The power consumption of the VM depends on the used state, i.e., on the number of active amplifiers. This results in 60 mW when all amplifiers are switched off, 145 mW when one amplifier is active and 225 mW when two amplifiers are active.

In phased-array applications, the phase differences between the antennas are important. While the absolute phase changes when fuses are removed, the phase difference stays nearly constant. Therefore, only the curve with no removed fuses is shown in Fig. 16. It can be seen that the phase curves are not equidistant to each other, as we saw with the simulation results.

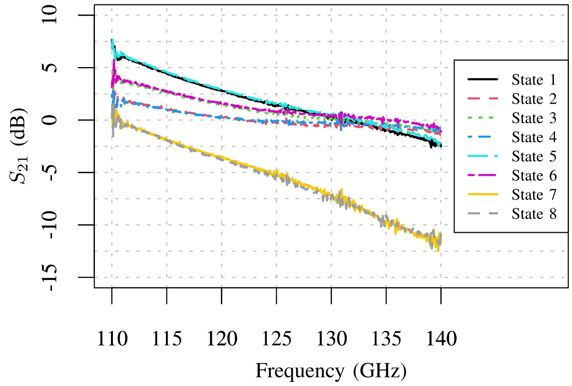

FIGURE 15. S_{21} **(dB) measurement results of the VM when two fuses are cut (compensated pad and balun losses).**

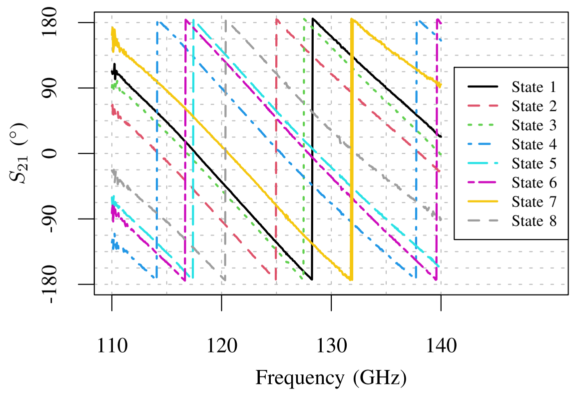

FIGURE 16. S_{21} **(°) measurement results of the VM when no fuses are cut.**

B. CONSTELLATION DIAGRAM AT 125 GHZ AND CORRECTION TECHNIQUE

As seen in the previous Section, the coupler's influence is not negligible. Therefore, theoretical investigations are performed here to determine the coupler's influence on the measurement results. For this purpose, a circuit simulation (similar to Fig. 2) is performed using the coupler's simulation results and an ideal VM with the S-parameter matrix shown in (3).

$$[S] = G_{I,Q} \begin{bmatrix} 0 & 0 & 0 & 0 & 0 & 0 \\ 0 & 0 & 0 & 0 & 0 & 0 \\ 0 & 0 & 0 & 0 & 0 & 0 \\ 0 & 0 & 0 & 0 & 0 & 0 \\ 1|0 & 0|1 & 1|0 & 0|1 & 0 & 0 \\ 0|1 & 1|0 & 0|1 & 1|0 & 0 & 0 \end{bmatrix} \qquad (3)$$

Here, a 6×6 linear-scaled matrix is used to describe an ideal VM, according to the circuit diagram in Fig. 1, with its four input ports and two output ports. Because it's a theoretical investigation, the return loss of the four input ports (U_{I+}, U_{I-}, U_{Q+}, and U_{Q-} - upper left matrix entries) and two output ports (U_{O+} and U_{O-} - lower right matrix entries) are 0. The lower left part of the matrix describes the transmission behavior of the VM. Depending on the state, the matrix entry is 0 or 1. Because of the built-in CMOS inverter and the cross-connected inductive load, the fifth and sixth row have swapped entries. Each of the four theoretical amplifiers has the same gain, namely $G_{I,Q}$.

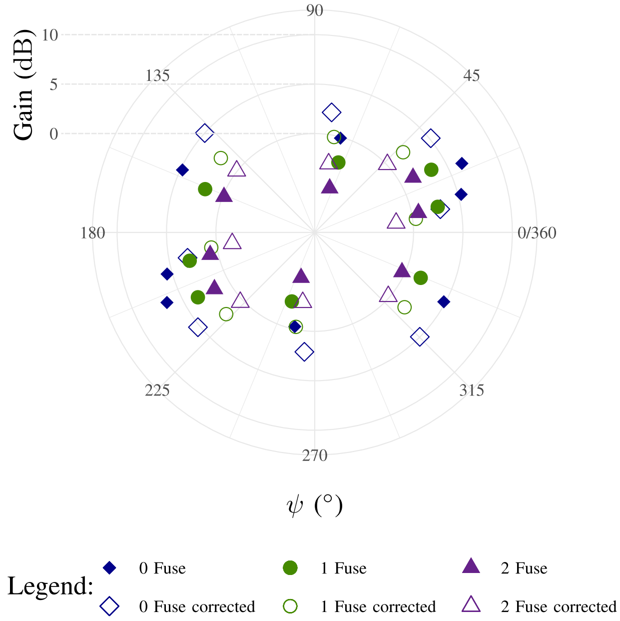

FIGURE 17. Constellation diagram of the VM for three different fuse configurations (filled symbols) including the corrected values (hollow symbols) at 125 GHz.

For every VM phase state, one touchstone S-parameter file is created. Inside the Cadence Virtuoso circuit diagram, the S-parameter data from the Sonnet simulations and one of the eight ideal VM touchstone files are used. Therefore, eight harmonic balance based S-parameter simulations must be performed. Here, $G_{I,Q}$ is set to 1 (unity-gain). With the sonnet simulation results and (3), the vector $\vec{v}_{coupler}$ is created, which contains only the non-ideal balun and branchline properties. Also, the vector $\vec{v}_{ideal}$ is created, which contains the ideal results when perfect couplers are used. With perfect IQ signals and $G_{I,Q} = 1$, the ideal vector is

$$\vec{v}_{ideal} = \Big(e^{j0^\circ}, \sqrt{2}e^{j45^\circ}, e^{j90^\circ}, \sqrt{2}e^{j135^\circ}, e^{j180^\circ}, \sqrt{2}e^{j225^\circ}, e^{j270^\circ}, \sqrt{2}e^{j315^\circ}\Big)^T. \qquad (4)$$

Now, the correction vector $\vec{v}_{corr}$ can be created (cf. Eq 5). With the correction vector, the measured data will be adjusted to separate coupler imperfections from VM imperfections.

The gain correction with the back-to-back structure (cf. Fig. 11) is not applicable since the baluns would be compensated twice. Therefore, only pad losses can be removed. Based on an additional measurement with back-to-back RF pads, the pad losses are ≈ 1.5 dB at 125 GHz.

$$\vec{v}_{corr} = \vec{v}_{ideal} - \vec{v}_{coupler} \qquad (5)$$

Fig. 17 shows the constellation diagram. On the one hand, it contains the measured S-parameter data at 125 GHz from the previous Section, and on the other hand, the corrected values. Here, the constellation points are arranged such as the RMS

TABLE 1. Key Parameters of the Constellation Diagram at 125 GHz

	RMSE (°)	RMSE (dB)	Min. Gain (dB)	Max. Gain (dB)	Avg. Gain (dB)
0F	16.91	2.57	−0.27	6.55	4.13
0F$^\sharp$	7.12	1.27	2.12	5.22	3.84
1F	17.85	2.37	−2.65	3.52	1.37
1F$^\sharp$	7.68	1.00	−0.26	2.19	1.08
2F	17.19	2.64	−5.29	1.65	−0.80
2F$^\sharp$	7.04	1.25	−2.91	0.32	−1.09

Note: $^\sharp$: After removing the coupler imperfections.

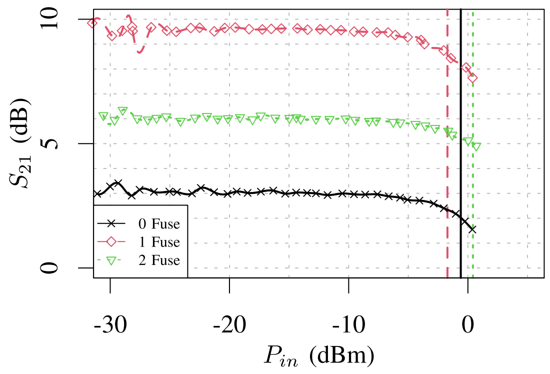

FIGURE 18. Gain compression of the VM at 110 GHz when no, one, and two laserfuses are cut (compensated pad and balun losses).

phase error is minimal. Therefore, state 1 is not aligned to 0°. The key parameters of the constellation diagram are listed in Table 1.

It can be seen that the measured gain decreases with each removed fuse. Furthermore, it can be seen that the correction method turns the constellation points in the right angular direction and corrects the IQ imbalance. The corrected values and especially their phases are now in very good agreement with the simulation results from Section III-C. Before the correction, the RMS deviations are ≈ 2.5 dB and ≈ 17°, respectively. After correction, the values have improved to ≈ 1.2 dB and ≈ 7°, respectively. By applying the correction method, the average gain drops by 0.29 dB because the measured pad losses and simulated coupler losses are lower than the measured losses of the back-to-back balun structure. Nevertheless, the corrected RMS values give a much better impression of the VM's performance and its usability in a radar system. In addition, now they fit well to the simulated RMS values (cf. Fig. 10).

C. COMPRESSION BEHAVIOR

Another aspect of a vector modulator is the compression behavior. To measure this, a slightly different VNA setup was used. This time, a Keysight extender (N5295AX03) with coaxial cables and a power sensor (Keysight U8489 A) are used. The calibration was performed up to 110 GHz. The recorded compression data are shown in Fig. 18.

At 110 GHz, the maximum gain is achieved with one cut fuse and is almost 10 dB, when I and Q are active. When two fuses are cut, ≈ 6 dB can be achieved, and ≈ 3 dB when no fuse is cut. The 1-dB input compression points are at −0.63 dBm, −1.74 dBm, and 0.45 dBm input power for the cases when no, one, or two fuses are removed. The compression points are plotted as vertical lines in Fig. 18.

D. COMPARISON WITH OTHER D-BAND VECTOR MODULATORS

Table 2 compares the VM presented here with other published VMs. The frequency range, technology, gain, (core) area, power consumption, input compression point, control interface, and the RMS amplitude and phase error are compared. The column with the area data shows that some designs use a lot of area. For example, structures are used where couplers and PA stages alternate. When comparing the core area, the VM presented here performs competitively. Also, it stands out in terms of gain (7.01 dB at ≈ 121 GHz and 6.55 dB at 125 GHz). Therefore, the VM creates no losses compared to others. While some VMs generate more gain, they use additional PA stages, which are not necessary for the basic functionality of the VM. Nevertheless, they can keep the power dissipation low. When looking at the compression points, the presented VM achieves the second-highest value.

The comparison of RMS errors is a bit difficult since the other VMs use analog control voltages. With high-resolution DACs, it is possible to achieve high accuracy. This is not achievable with a digital approach since no analog retuning is possible. Nevertheless, deviations of 2.57 dB and 16.91° or 1.27 dB and 7.12°, after removing the coupler imperfections, can be achieved.

V. PHASED-ARRAY INVESTIGATIONS AT 125 GHZ

Nowadays, the concept of virtual antennas ensures that a large virtual array can be created with only a few physical Tx and Rx antennas. This means that the detection performance can exceed that of a phased-array system with the same number of antennas [70], [71]. However, the phased-array approach offers a distinct advantage. By combining the Tx antennas, the radiated power can be increased proportionally with the number of antennas. Phase-shifters are required for beam-steering, where accurate angular resolution is often desired.

The presented VM has only eight phase states with a phase difference of ≈ 45°. The ninth state, where the VM is turned off, is not considered. Nevertheless, the VM can be used to perform finely resolved beam steering. In Fig. 19, the array factor is shown for three different scenarios where the antenna count N is 2, 4, or 6.

The antennas are arranged linearly at a spacing of $\lambda/2$, i.e., as a uniform linear array (ULA) at the locations $\vec{r}$. The antennas are fed by identical VMs, which have the same

TABLE 2. State of the Art SiGe BiCMOS Based Vector Modulators at Frequencies Above 100 GHz

Ref.	Frequency (GHz)	Tech.	Area (mm^2)	Peak Gain (dB)	P_{DC} (mW)	$P_{1\,dB}$ (dBm)	Control	RMS Amplitude (dB)	RMS Phase (°)
[33]	140−200	130 nm	0.26‡	10♠ (3, 5♠c)	28	—	analog	< 3	< 10
[32]	115	130 nm	2.11	0.5♣	33♣	−22 (IP)♣	analog	< 1.6	< 5.5
[36]	92−100	130 nm	0.853‡	9.5♠a :	50	−26 (IP)	analog	< 1.8	< 5
[38]	113−127	130 nm	0.05‡	18.7♠	225	0.7 (OP)	analog	—	—
[42]	110−130	250 nm	—	−10♠	148	−9 (OP)	analog	—	—
[44]	220−250	130 nm	—	−8♣	106	−5 (IP)♣	analog	—	—
[48]	140−160	55 nm	0.05‡	−4.5	50	2 (IP)	analog	< 1.4	< 7.5
[49]	162−190	130 nm	0.07‡	−6.2	12.4	−13.5 (IP)♣	analog	< 1	< 8
[59]	160−200	130 nm	0.075‡	−9.5	8.6	—	analog	< 0.9	< 15
[66]	75−100	130 nm	—	−5♣	—	−2 (IP)♣	on-chip DAC	< 1	< 7.5
This	110−140	130 nm	0.086‡,nr	6.55 (4.13a)	60−225	−0.63 (IP)◇	digital	2.57	16.91
This♯	110−140	130 nm	0.086‡,nr	5.22 (3.84a)	60−225	—	digital	1.27	7.12

Note: ‡: core area, ♠: with additional amplifiers, c : contentious 360° gain, a : average, ♣ : simulated, ◇ : at 110 GHz, ♯ : after removing the coupler imperfections, nr : non-rectangular size: 0.061 mm²

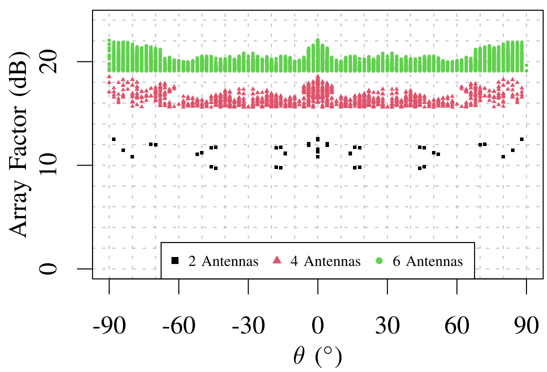

FIGURE 19. Simulated array factor at 125 GHz using the uncorrected measured *S*-parameter data when no fuse is cut.

design parameters and, therefore, the same imperfections. The uncorrected and measured S-parameter data at 125 GHz in the form of linear amplitude A and the phase ψ are used (cf. Fig 17) to calculate the array factor according to (6) [72, p. 293].

$$F_{dB}(m) = 20 \cdot log_{10}\left[\sum_{n=1}^{N} A(n,m) \cdot e^{j\psi(n,m)} \cdot e^{j\cdot k_0 \vec{r}(n)\cdot sin(\theta)\cdot cos(\varphi_0)}\right] \quad (6)$$

Here, k_0 is the wavenumber, and j is the imaginary number. For the elevation angle θ, a step size of $\Delta\theta = 2^\circ$ is used. The azimuth angle φ_0 is fixed at 0°. All combinations $m \in M$ for N antennas and $S = 8$ VM states are evaluated. In the simulation, the number of combinations increases exponentially and starts at $M = N^S = 2^8 = 256$ for two antennas and increases to 1,679,616 for six antennas.

Eq. (6) is used to calculate the array factor for the angle range from −90° to 90° for each combination. In Fig. 19, the maximum value and its angular position, i.e., the array factor of the main lobe, is entered as a point. All calculated main lobes (points) are removed that are 3 dB below the maximum at $\theta = 0^\circ$ to keep the plot readable. The beam-steering capabilities improve significantly with the number of antennas. With two antennas, the ≈ 45° phase resolution is visible. But when increasing the antenna count to four antennas, the beam can be continuously steered in the whole angular spectrum. Increasing the number of antennas from four to six shows minor improvements in the variation of the array factor (< 2 dB).

VI. PHASE-CODED RADAR INVESTIGATIONS AT 125 GHZ

Besides FMCW radar, research on PMCW radar increases because it has improved interference properties [19], [73], [74], [75]. This is important in environments with many radar sensors, such as the automotive industry. However, this increases the effort for signal sampling and digital demodulation [17], [18].

The PMCW performance is simulated using RC parasitics and the coupler's S-parameter because the breakout MMIC has no mixer. We focus on the phase states I + Q and −I − Q as they have ≈ 180° phase difference (cf. Sec. IV-B), and the same power consumption. The digital interface of the VM (D_I, D_Q) is driven with a pseudo-noise bit sequence with a chip rate of $B_c = 0.25$ GHz, and the output of the VM is connected to an ideal mixer with 10 dB conversion gain. The mixer and the VM share the same mono-frequent 125 GHz LO signal.

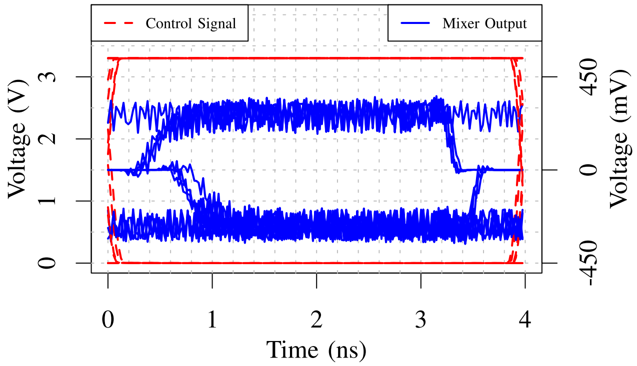

FIGURE 20. Simulated eye diagram at 125 GHz of the VM using the sonnet simulation data and RC parasitics.

Fig. 20 shows the transient IF signal of the mixer in form of an eye diagram. It can be seen that the down-converted signal has a wide-open eye. A further increase of the chip rate would enhance the range resolution ($\Delta r = c/(2 \cdot B_c)$) [18]. But, this leads to a reduction of the eye size and to signals that can no longer be detected properly.

VII. CONCLUSION

This article presented a 125 GHz SiGe-based vector modulator that is characterized by its simple digital interface, and by its high gain in the D-band of up to 10 dB at 110 GHz and up to 6.55 dB at 125 GHz. In comparison, most other VMs produce only losses in the D-band. In addition, a technique to isolate the coupler's imperfections was presented, which leads to an RMS phase error of 7.12°, and an RMS amplitude error of 1.27 dB.

Besides the simulation and measurement results, its applicability in phased-array FMCW and phased-coded CW systems were also shown. A variance of the array factor of less than 2 dB was achieved while having full coverage of the elevation angle. Here, the measured S-parameter data and an ULA with six antennas were used. Even with only four antennas, very good coverage is achieved. In addition, the VM can also be used in a phase-coded system and operated with a modulation frequency of 0.25 GHz. For both types of operation, no DAC is needed, which reduces PCB size, power consumption, and the system's complexity and cost when large-scale arrays are used. These two modes are possible in addition to the classic TDM method without changing the hardware by fuses or a complete replacement.

Future research should focus on higher switching speeds to enhance the PMCW capabilities, and on investigating the DDMA properties. In summary, the VM adds significantly more flexibility to current radar systems to achieve the best possible detection accuracy in a wide range of environmental conditions.

ACKNOWLEDGMENT

The authors are grateful to Infineon Technologies AG for manufacturing and providing the breakout chip with the vector modulator and to Klaus Aufinger, Infineon Technologies AG, for his extensive and valuable consultation.

REFERENCES

[1] C. Waldschmidt, J. Hasch, and W. Menzel, "Automotive radar from first efforts to future systems," *IEEE J. Microwaves*, vol. 1, no. 1, pp. 135–148, Jan. 2021.
[2] B. Sene, D. Reiter, H. Knapp, H. Li, T. Braun, and N. Pohl, "An automotive D-band FMCW radar sensor based on a SiGe-transceiver MMIC," *IEEE Microw. Wireless Compon. Lett.*, vol. 32, no. 3, pp. 194–197, Mar. 2022.
[3] M. Köhler, J. Hasch, H. L. Blöcher, and L.-P. Schmidt, "Feasibility of automotive radar at frequencies beyond 100 GHz," *Int. J. Microw. Wireless Technol.*, vol. 5, no. 1, pp. 49–54, Dec. 2012.
[4] T. Jaeschke, S. Kueppers, N. Pohl, and J. Barowski, "Calibrated and frequency traceable d-band FMCW radar for VNA-like s-parameter measurements," in *Proc. IEEE Radio Wireless Symp.*, Las Vegas, NV, USA, 2022, pp. 64–67.
[5] P. Stadler, H. Papurcu, T. Welling, S. T. Alfageme, and N. Pohl, "An overview of state-of-the-art D-band radar system components," *Chips*, vol. 1, no. 3, pp. 121–149, 2022.
[6] H. L. van Trees, *Optimum Array Processing: Part IV of Detection, Estimation, and Modulation Theory*. Hoboken, NJ, USA: Wiley, 2002.
[7] J. Wittemeier, A. M. Ahmed, T. N. Tran, A. Sezgin, and N. Pohl, "3D localization using a scalable FMCW MIMO radar design," in *Proc. 13th German Microw. Conf.*, Cottbus, Germany, 2020, pp. 100–103.
[8] P. Hillger et al., "Toward mobile integrated electronic systems at THz frequencies," *J. Infrared Millimeter THz Waves*, vol. 41, no. 7, pp. 846–869, Jun. 2020.
[9] D. Kissinger, G. Kahmen, and R. Weigel, "Millimeter-wave and terahertz transceivers in SiGe BiCMOS technologies," *IEEE Trans. Microw. Theory Techn.*, vol. 69, no. 10, pp. 4541–4560, Oct. 2021.
[10] J. Wittemeier, F. Vogelsang, D. Starke, H. Rücker, and N. Pohl, "A SiGe based 0.48 THz signal source with 45 GHz tuning range," in *Proc. 51st Eur. Microw. Conf.*, London, U.K., 2022, pp. 869–872.
[11] D. Starke et al., "A fully integrated 0.48 THz FMCW radar transceiver MMIC in a SiGe-technology," in *Proc. 17th Eur. Microw. Integr. Circuits Conf.*, Milan, Italy, 2022, pp. 56–59.
[12] S. H. Dokhanchi, B. S. Mysore, K. V. Mishra, and B. Ottersten, "A mmWave automotive joint radar-communications system," *IEEE Trans. Aerosp. Electron. Syst.*, vol. 55, no. 3, pp. 1241–1260, Jun. 2019.
[13] F. Liu, C. Masouros, A. P. Petropulu, H. Griffiths, and L. Hanzo, "Joint radar and communication design: Applications, state-of-the-art, and the road ahead," *IEEE Trans. Commun.*, vol. 68, no. 6, pp. 3834–3862, Jun. 2020.
[14] L. G. de Oliveira, B. Nuss, M. B. Alabd, A. Diewald, M. Pauli, and T. Zwick, "Joint radar-communication systems: Modulation schemes and system design," *IEEE Trans. Microw. Theory Techn.*, vol. 70, no. 3, pp. 1521–1551, Nov. 2022.
[15] W. Lee, T. Dinc, and A. Valdes-Garcia, "Multi-mode 60-GHz radar transmitter SoC in 45-nm SOI CMOS," *IEEE J. Solid-State Circuits*, vol. 55, no. 5, pp. 1187–1198, May 2020.
[16] G. Rubio-Cidre, A. Badolato, L. Ú. Medina, J. Grajal, B. Mencia-Oliva, and B.-P. Dorta-Naranjo, "DDS-based signal-generation architecture comparison for an imaging radar at 300 GHz," *IEEE Trans. Instrum. Meas.*, vol. 64, no. 11, pp. 3085–3098, Nov. 2015.
[17] G. Hakobyan and B. Yang, "High-performance automotive radar: A review of signal processing algorithms and modulation schemes," *IEEE Signal Process. Mag.*, vol. 36, no. 5, pp. 32–44, Sep. 2019.
[18] D. Guermandi et al., "A 79-GHz 2 × 2 MIMO PMCW radar SoC in 28-nm CMOS," *IEEE J. Solid-State Circuits*, vol. 52, no. 10, pp. 2613–2626, Oct. 2017.
[19] X. Shang, J. Li, and P. Stoica, "Weighted SPICE algorithms for range-Doppler imaging using one-bit automotive radar," *IEEE J. Sel. Topics Signal Process.*, vol. 15, no. 4, pp. 1041–1054, Jun. 2021.
[20] F. Roos, J. Bechter, C. Knill, B. Schweizer, and C. Waldschmidt, "Radar sensors for autonomous driving: Modulation schemes and interference mitigation," *IEEE Microw. Mag.*, vol. 20, no. 9, pp. 58–72, Sep. 2019.
[21] F. Xu, S. A. Vorobyov, and F. Yang, "Transmit beamspace DDMA based automotive MIMO radar," *IEEE Trans. Veh. Technol.*, vol. 71, no. 2, pp. 1669–1684, Feb. 2022.

[22] S. Kueppers, H. Cetinkaya, R. Herschel, and N. Pohl, "A compact 24×24 channel MIMO FMCW radar system using a substrate integrated waveguide-based reference distribution backplane," *IEEE Trans. Microw. Theory Techn.*, vol. 68, no. 6, pp. 2124–2133, Jun. 2020.
[23] S. Kueppers, H. Cetinkaya, and N. Pohl, "A compact 120 GHz SiGe:C based 2 x 8 FMCW MIMO radar sensor for robot navigation in low visibility environments," in *Proc. Eur. Radar Conf.*, Nuremberg, Germany, 2017, pp. 122–125.
[24] R. Feger, C. Wagner, S. Schuster, S. Scheiblhofer, H. Jager, and A. Stelzer, "A 77-GHz FMCW MIMO radar based on an SiGe single-chip transceiver," *IEEE Trans. Microw. Theory Techn.*, vol. 57, no. 5, pp. 1020–1035, May 2009.
[25] A. Ganis et al., "A portable 3-D imaging FMCW MIMO radar demonstrator with a 24×24 antenna array for medium-range applications," *IEEE Trans. Geosci. Remote Sens.*, vol. 56, no. 1, pp. 298–312, Jan. 2018.
[26] W. A. Ahmad et al., "Multimode W-band and D-band MIMO scalable radar platform," *IEEE Trans. Microw. Theory Techn.*, vol. 69, no. 1, pp. 1036–1047, Jan. 2021.
[27] H. Haderer, R. Feger, C. Pfeffer, and A. Stelzer, "Millimeter-wave phase-coded CW MIMO radar using zero- and low-correlation-zone sequence sets," *IEEE Trans. Microw. Theory Techn.*, vol. 64, no. 12, pp. 4312–4323, Dec. 2016.
[28] R. Feger, H. Haderer, H. J. Ng, and A. Stelzer, "Realization of a sliding-correlator-based continuous-wave pseudorandom binary phase-coded radar operating in w-band," *IEEE Trans. Microw. Theory Techn.*, vol. 64, no. 10, pp. 3302–3318, Oct. 2016.
[29] A. Natarajan, A. Valdes-Garcia, B. Sadhu, S. K. Reynolds, and B. D. Parker, "W-band dual-polarization phased-array transceiver front-end in SiGe BiCMOS," *IEEE Trans. Microw. Theory Techn.*, vol. 63, no. 6, pp. 1989–2002, Jun. 2015.
[30] A. Natarajan, A. Komijani, X. Guan, A. Babakhani, and A. Hajimiri, "A 77-GHz phased-array transceiver with on-chip antennas in silicon: Transmitter and local LO-path phase shifting," *IEEE J. Solid-State Circuits*, vol. 41, no. 12, pp. 2807–2819, Dec. 2006.
[31] A. Townley et al., "A 94-GHz 4TX–4RX phased-array FMCW radar transceiver with antenna-in-package," *IEEE J. Solid-State Circuits*, vol. 52, no. 5, pp. 1245–1259, May 2017.
[32] S. Afroz and K.-J. Koh, "A D-band two-element phased-array receiver front end with quadrature-hybrid-based vector modulator," *IEEE Microw. Wireless Compon. Lett.*, vol. 28, no. 2, pp. 180–182, Feb. 2018.
[33] P. Stärke, V. Rieß, C. Carta, and F. Ellinger, "Continuous 360° vector modulator with passive phase generation for 140 GHz to 200 GHz G-Band," in *Proc. 12th German Microw. Conf.*, Stuttgart, Germany, 2019, pp. 240–243.
[34] S. Afroz and K.-J. Koh, "90 hybrid-coupler based phase-interpolation phase-shifter for phased-array applications at w-band and beyond," in *Proc. IEEE MTT-S Int. Microw. Symp.*, San Francisco, CA, USA, 2016, pp. 1–4.
[35] S. Afroz, H. Kim, and K.-J. Koh, "Power-efficient W-band (92–98 GHz) phased-array transmit and receive elements with quadrature-hybrid-based passive phase interpolator," *IEEE J. Solid-State Circuits*, vol. 53, no. 6, pp. 1678–1693, Jun. 2018.
[36] S. Afroz and K.-J. Koh, "W-band (92–100 GHz) phased-array receive channel with quadrature-hybrid-based vector modulator," *IEEE Trans. Circuits Syst. I*, vol. 65, no. 7, pp. 2070–2082, Jul. 2018.
[37] H. Li, J. Chen, D. Hou, and W. Hong, "A W-band 6-bit phase shifter with 7 dB gain and 1.35 RMS phase error in 130 nm SiGe BiCMOS," *IEEE Trans. Circuits Syst. II*, vol. 67, no. 10, pp. 1839–1843, Oct. 2020.
[38] E. Öztürk, H. Ng, W. Winkler, and D. Kissinger, "$0.1 mm^2$ SiGe BiCMOS RX / TX channel front-ends for 120 GHz phased array radar systems," in *Proc. IEEE 17th Top. Meeting Silicon Monolithic Integr. Circuits RF Syst.*, Phoenix, AZ, USA, 2017, pp. 50–53.
[39] S. Y. Kim, D.-W. Kang, K.-J. Koh, and G. M. Rebeiz, "An improved widebandall-pass I/Q network for millimeter-wave phase shifters," *IEEE Trans. Microw. Theory Techn.*, vol. 60, no. 11, pp. 3431–3439, Nov. 2012.
[40] Y. Sun and C. J. Scheytt, "A 360 degree phase shifter for 60 GHz application in SiGe BiCMOS technology," in *Proc. IEEE Int. Conf. Microw., Comm., Antennas Electron. Syst*, Tel Aviv, Israel, 2009, pp. 1–4.
[41] I. Sarkas, M. Khanpour, A. Tomkins, P. Chevalier, P. Garcia, and S. P. Voinigescu, "W-band 65-nm CMOS and SiGe BiCMOS transmitter and receiver with lumped I-Q phase shifters," in *Proc. IEEE Radio Freq. Integr. Circuits Symp.*, Boston, MA, USA, 2009, pp. 441–444.
[42] M. Elkhouly, S. Glisic, F. Ellinger, and J. C. Scheytt, "120 GHz phased-array circuits in $0.25 \mu m$ SiGe BiCMOS technology," in *Proc. 7th German Microw. Conf.*, Ilmenau, Germany, Mar. 2012, pp. 1–4.
[43] M. Elkhouly, C.-S. Choi, S. Glisic, F. Ellinger, and J. C. Scheytt, "A 60 GHz eight-element phased-array receiver front-end in 0.25 μm SiGe BiCMOS technology," *Int. J. Microw. Wireless Technol.*, vol. 4, no. 6, pp. 579–594, Sep. 2012.
[44] M. Elkhouly, S. Glisic, C. Meliani, F. Ellinger, and J. C. Scheytt, "220–250-GHz phased-array circuits in 0.13-μm SiGe BiCMOS technology," *IEEE Trans. Microw. Theory Techn.*, vol. 61, no. 8, pp. 3115–3127, Aug. 2013.
[45] K. E. Drenkhahn, A. Gadallah, A. Franzese, C. Wagner, and A. Malignaggi, "A V-band vector modulator based phase shifter in BiCMOS $0.13 \mu m$ SiGe technology," in *Proc. 15th Europ. Microw. Integr. Circuits Conf.*, Utrecht, Netherlands, 2021, pp. 65–68.
[46] H. Li, J. Chen, D. Hou, Z. Li, R. Zhou, and W. Hong, "A 94 GHz scalable 2×2 phased-array receiver in SiGe BiCMOS for high data-rate communication," in *Proc. IEEE Custom Integr. Circuits Conf.*, Austin, TX, USA, 2021, pp. 1–2.
[47] M. Kantanen, J. Holmberg, and T. Karttaavi, "Two-way vector modulator SiGe MMIC for millimeter-wave phased array applications," in *Proc. Glob. Symp. Millim.-Waves*, Montreal, QC, Canada, 2015, pp. 1–3.
[48] D. del Rio, I. Gurutzeaga, R. Berenguer, I. Huhtinen, and J. F. Sevillano, "A compact and high-linearity 140–160 GHz active phase shifter in 55 nm BiCMOS," *IEEE Microw. Wireless Compon. Lett.*, vol. 31, no. 2, pp. 157–160, Feb. 2021.
[49] P. V. Testa, C. Carta, and F. Ellinger, "A 160–190-GHz vector-modulator phase shifter for low-power applications," *IEEE Microw. Wireless Compon. Lett.*, vol. 30, no. 1, pp. 86–89, Jan. 2020.
[50] B. Welp, A. Meusling, K. Aufinger, and N. Pohl, "A mixed-mode beamforming radar transmitter MMIC utilizing novel ultrawideband IQ-generation techniques in SiGe BiCMOS," *IEEE Trans. Microw. Theory Techn.*, vol. 66, no. 6, pp. 2604–2617, Mar. 2018.
[51] J.-O. Plouchart et al., "A fully-integrated 94-GHz 32-element phased-array receiver in SiGe BiCMOS," in *Proc. IEEE Radio Freq. Integr. Circuits Symp.*, Honolulu, HI, USA, 2017, pp. 380–383.
[52] T.-W. Li and H. Wang, "A millimeter-wave fully integrated passive reflection-type phase shifter with transformer-based multi-resonance loads for 360 phase shifting," *IEEE Trans. Circuits Syst. I*, vol. 65, no. 4, pp. 1406–1419, Apr. 2018.
[53] A. Valdes-Garcia et al., "A fully integrated 16-element phased-array transmitter in SiGe BiCMOS for 60-GHz communications," *IEEE J. Solid-State Circuits*, vol. 45, no. 12, pp. 2757–2773, Dec. 2010.
[54] W. Lee et al., "Fully integrated 94-GHz dual-polarized TX and RX phased array chipset in SiGe BiCMOS operating up to 105°C," *IEEE J. Solid-State Circuits*, vol. 53, no. 9, pp. 2512–2531, Sep. 2018.
[55] M. Kantanen, J. Holmberg, M. Varonen, and A. Rantala, "Digitally controlled vector modulator SiGe MMIC for millimeter-wave phased array applications," in *Proc. 11th German Microw. Conf.*, Freiburg, Germany, 2018, pp. 51–54.
[56] B.-H. Ku, O. Inac, M. Chang, H.-H. Yang, and G. M. Rebeiz, "A high-linearity 7685-GHz 16-element 8-transmit/8-receive phased-array chip with high isolation and flip-chip packaging," *IEEE Trans. Microw. Theory Techn.*, vol. 62, no. 10, pp. 2337–2356, Oct. 2014.
[57] S. Y. Kim and G. M. Rebeiz, "A low-power BiCMOS 4-element phased array receiver for 76–84 GHz radars and communication systems," *IEEE J. Solid-State Circuits*, vol. 47, no. 2, pp. 359–367, Feb. 2012.
[58] K. Greene, A. Sarkar, and B. Floyd, "A 60-GHz dual-vector Doherty beamformer," *IEEE J. Solid-State Circuits*, vol. 52, no. 5, pp. 1373–1387, May 2017.
[59] P. V. Testa, C. Carta, and F. Ellinger, "A 140–210 GHz low-power vector-modulator phase shifter in 130 nm SiGe BiCMOS technology," in *Proc. Asia-Pacific Microw. Conf.*, Kyoto, Japan, 2018, pp. 530–532.
[60] T. Ross, S. Tiller, K. Ansari, and M. Repeta, "A 6-bit phase shifter at E-band using a feedback-controlled variable attenuator," in *Proc. 48th Euro. Microw. Conf.*, Madrid, Spain, 2018, pp. 800–803.
[61] A. Tomkins, R. A. Aroca, T. Yamamoto, S. T. Nicolson, Y. Doi, and S. P. Voinigescu, "A zero-IF 60 GHz 65 nm CMOS transceiver with direct BPSK modulation demonstrating up to 6 Gb/s data rates over a 2 m wireless link," *IEEE J. Solid-State Circuits*, vol. 44, no. 8, pp. 2085–2099, Aug. 2009.

[62] M. Furqan, F. Ahmed, R. Feger, K. Aufinger, and A. Stelzer, "A 122-GHz system-in-package radar sensor with BPSK modulator in a 130-nm SiGe BiCMOS technology," in *Proc. 46th Eur. Microw. Conf.*, London, U.K., 2016, pp. 683–686.

[63] H. J. Ng, M. Kucharski, W. Ahmad, and D. Kissinger, "Multi-purpose fully differential 61- and 122-GHz radar transceivers for scalable MIMO sensor platforms," *IEEE J. Solid-State Circuits*, vol. 52, no. 9, pp. 2242–2255, Sep. 2017.

[64] V. Issakov, A. Bilato, V. Kurz, D. Englisch, and A. Geiselbrechtinger, "A highly integrated D-band multi-channel transceiver chip for radar applications," in *Proc. IEEE BiCMOS Compound Semicond. Integr. Circuits Technol. Symp.*, Nashville, TN, USA, 2019, pp. 1–4.

[65] M. Elkhouly, C.-S. Choi, S. Glisic, C. Scheytt, and F. Ellinger, "Millimeter-wave beamforming circuits in SiGe BiCMOS," in *Proc. IEEE Bipolar/BiCMOS Circuits Technol. Meeting*, Austin, TX, USA, 2010, pp. 129–132.

[66] F. Golcuk, T. Kanar, and G. M. Rebeiz, "A 90–100-GHz 4 x 4 SiGe BiCMOS polarimetric transmit/receive phased array with simultaneous receive-beams capabilities," *IEEE Trans. Microw. Theory Techn.*, vol. 61, no. 8, pp. 3099–3114, Aug. 2013.

[67] F. Vogelsang, D. Starke, J. Wittemeier, H. Rücker, and N. Pohl, "A highly-efficient 120 GHz and 240 GHz signal source in a SiGe-technology," in *Proc. IEEE BiCMOS Compound Semicond. Integr. Circuits Technol. Symp.*, Monterey, CA, USA, 2020, pp. 1–4.

[68] J. Rautio and V. Demir, "Microstrip conductor loss models for electromagnetic analysis," *IEEE Trans. Microw. Theory Techn.*, vol. 51, no. 3, pp. 915–921, Mar. 2003.

[69] S. Belkin, "Differential circuit characterization with two-port s-parameters," *IEEE Microw. Mag.*, vol. 7, no. 6, pp. 86–99, Dec. 2006.

[70] A. Hassanien and S. A. Vorobyov, "Phased-MIMO radar: A tradeoff between phased-array and MIMO radars," *IEEE Trans. Signal Process.*, vol. 58, no. 6, pp. 3137–3151, Jun. 2010.

[71] J. Li and P. Stoica, "MIMO radar with colocated antennas," *IEEE Signal Process. Mag.*, vol. 24, no. 5, pp. 106–114, Sep. 2007.

[72] C. A. Balanis, *Antenna Theory*. Hoboken, NJ, USA: Wiley, Apr. 2016.

[73] R. Lin, M. Soltanalian, B. Tang, and J. Li, "Efficient design of binary sequences with low autocorrelation sidelobes," *IEEE Trans. Signal Process.*, vol. 67, no. 24, pp. 6397–6410, Dec. 2019.

[74] S. Alland, W. Stark, M. Ali, and M. Hegde, "Interference in automotive radar systems: Characteristics, mitigation techniques, and current and future research," *IEEE Signal Process. Mag.*, vol. 36, no. 5, pp. 45–59, Sep. 2019.

[75] S. Sun, A. P. Petropulu, and H. V. Poor, "MIMO radar for advanced driver-assistance systems and autonomous driving: Advantages and challenges," *IEEE Signal Process. Mag.*, vol. 37, no. 4, pp. 98–117, Jul. 2020.

JONATHAN WITTEMEIER (Graduate Student Member, IEEE) was born in Lünen, Germany. He received the B.Sc. and M.Sc. degrees in electrical engineering and information technology from Technical University Dortmund, Dortmund, Germany, in 2014 and 2016, respectively. Between 2016 and 2017, he was with the automotive industry as a Software Developer. Since 2017, he has been a Research Assistant with the Institute of Integrated Systems, Ruhr University Bochum, Bochum, Germany. His research interests include mm-wave radar, MMIC design using Silicon-Germanium, and MIMO algorithms.

MUHAMMED ALI YILDIRIM (Graduate Student Member, IEEE) was born in Essen, Germany. He received the B.Sc. and M.Sc. degrees in electrical engineering and information technology from Ruhr-University Bochum, Bochum, Germany, in 2019 and 2022, respectively. Since 2022, he has been a Research Assistant with the Institute of Integrated Systems, Ruhr-University Bochum. His research interests include mm-wave radar and MMIC design using silicon-germanium.

NILS POHL (Senior Member, IEEE) received the Dipl.-Ing. and Dr.-Ing. degrees in electrical engineering from Ruhr University Bochum, Bochum, Germany, in 2005 and 2010, respectively. From 2006 to 2011, he was a Research Assistant with Ruhr University Bochum, where he was involved in integrated circuits for millimeter-wave (mm-wave) radar applications. In 2011, he became an Assistant Professor with Ruhr University Bochum. In 2013, he became the Head of the Department of mm-wave Radar and High Frequency Sensors with the Fraunhofer Institute for High Frequency Physics and Radar Techniques, Wachtberg, Germany. In 2016, he became a Full Professor of integrated systems with Ruhr University Bochum. He has authored or coauthored more than 100 scientific papers and has issued several patents. His research interests include ultrawideband mm-wave radar, design, and optimization of mm-wave integrated SiGe circuits and system concepts with frequencies up to 300 GHz and above, and frequency synthesis and antennas. Prof. Pohl is a member of VDE, ITG, EUMA, and URSI. He was a co-recipient of the 2009 EEEfCom Innovation Award, the 2012 EuMIC Prize, and the 2015 Best Demo Award of the IEEE Radio Wireless Week, and a recipient of the Karl-Arnold Award of the North Rhine-Westphalian Academy of Sciences, Humanities and the Arts in 2013 and the IEEE MTT Outstanding Young Engineer Award in 2018.